



Research article

Symmetry break in the eight bubble compaction[†]

Giulia Bevilacqua*

MOX – Politecnico di Milano, Piazza Leonardo da Vinci 32, Milano, Italy

[†] **This contribution is part of the Special Issue:** Fluid instabilities, waves and non-equilibrium dynamics of interacting particles

Guest Editors: Roberta Bianchini; Chiara Saffirio

Link: www.aimspress.com/mine/article/5859/special-articles

* **Correspondence:** Email: giulia.bevilacqua1993@gmail.com.

Abstract: Geometry and mechanics have both a relevant role in determining the three-dimensional packing of 8 bubbles displayed in a similar foam structure. We assume that the spatial arrangement of bubbles obeys a geometrical principle maximizing the minimum mutual distance between the bubble centroids. The compacted structure is then obtained by radially packing the bubbles under constraint of volume conservation. We generate a polygonal tiling on the central sphere and peripheral bubbles with both flat and curved interfaces. We verify that the obtained polyhedra is optimal under suitable physical criteria. Finally, we enforce the mechanical balance imposing the constraint of conservation of volume. We find an anisotropy in the distribution of the field of forces: surface tensions of bubble-bubble interfaces with normal oriented in the circumferential direction of bubbles aggregate are larger than the ones with normal unit vector pointing radially out of the aggregate. We suggest that this mechanical cue is key for the symmetry break of this bubbles configuration.

Keywords: symmetry break; optimal tessellation; heptahedron; mechanical balance; anisotropy

1. Introduction

Often used for children's enjoyment, soap bubbles are the simplest physical example of a lot of mathematical problems. They are solutions of the minimal surface problem [1]: the connection between soap films and minimal surfaces was established by Gauss in 1830. Indeed, working on capillarity problems, he found that at equilibrium any liquid surface minimizes the potential energy caused by molecular forces. In the specific case of soap films, such a energy is proportional to the area. Hence, soap films are nothing but the physical representation of stable minimal surfaces. Then, soap bubbles are used to study two dimensional hydrodynamics and turbulence [2]: their use is

motivated by the fact that atmospheric turbulence at large scales displays two dimensional features due to the small thickness of the Earth's atmosphere [3]. Indeed, to mimic the emergence of hurricanes or cyclones in the atmosphere [4], which are the manifestation of turbulence, a half bubble is heated at the equator giving rise to thermal convection which leads, under some physical conditions, the appearance of the searched long lived isolated vortices [5]. Finally, they solve an optimization problem [6]: when two or more bubbles cluster together, their configuration obeys some physical optimization rules. Indeed, assembling several bubbles traps pockets of gas in a liquid and results in *foam*: the surfactants added to the liquid stabilize the bubbles by reducing the surface tension and by arranging themselves at the liquid/gas interfaces [7].

Regarding the behavior of a single soap bubble, everything is known. What is not completely understood is the geometrical and mechanical properties of a cluster of many bubbles, known as a foam. For instance, its optimal rearrangement in space is still matter of debate.

In 2D there are more results: Hales proved the *honeycomb conjecture*, which states that the partition of the plane into regular hexagons of equal area has least perimeter, i.e., it minimizes the perimeter fixing the area [8]. In this context, it has been proved that the optimal (i.e., minimal) configuration exists for N clusters [9, 10] and Cox et al., obtained their numerical visualizations up to $N = 200$ [11]. Due to the non linearity of the problem, in a lot of physical situations, the equilibrium solution is only stable with respect to *small displacements*, i.e., it is not a global minimum of the system. This aspect leads to mechanical instabilities which break the symmetry of the system [12–14]. These instabilities should be classified into two groups [15]: the first one is primarily due to the presence of an asymmetry in the system and it can be studied though a purely static model. For the second one, the system jumps away from this initial configuration to settle in another which is not close to it and its description may require a dynamic model. Just to mention some famous instabilities, we recall the $T1$ process in 2-dimension [16], and the $2D$ flower cluster [13].

If we move to 3D, the problem is minimizing the area functional and few exact result exist. The only rigorous one is the proof of *the Double Bubble Conjecture* [17], which states that the standard double bubble provides the least-area enclose and separates two regions of prescribed volume in \mathbb{R}^3 . As regarding the numerical results, Kelvin [18] proposed an optimal candidate structure with *identical cells*, which has been numerically refuted in [19]: by numerical calculations, an agglomerate of two different types of bubbles has less perimeter, for fixed area.

The aim of this work is to study the symmetry break of a eight bubble compaction in 3D, i.e., we want to investigate the mechanical cues driving the three-dimensional packing of 8 bubbles displayed in a recalling foam structure. To circumvent the difficulty of a variational approach, i.e., the minimization of an area functional satisfying some geometrical constraints, we follow a different strategy. First of all, in Section 2, we fix the geometrical arrangement of the eight bubbles as the solution of the Tamme's problem [20]: we exploit a geometrical principle of maximal mutual distance between neighbor points on a spherical surface obtaining seven symmetrical peripheral spheres tangent to the central one [21]. Then, compaction is produced by packing the outer bubbles along the radial direction of the aggregate. The obtained agglomerate recalls the foam structure [22]: the central sphere is completely covered, while the peripheral ones have a free-curved surface. While our construction does not ensure that the obtained final configuration is the minimal one, we will prove that the our tessellation on the central sphere is the optimal one among all the possible [23] according to physical assumptions: the liquid/liquid interface is favored versus the liquid/gas one and it maximizes the volume [7]. Fixing

the geometrical arrangement, in Section 3, we look for the balance of forces that produces such a configuration [6]. Enforcing the mechanical equilibrium and the conservation of volume, we derive the tensional balance laws on this geometrically optimal packing. Finally, in Section 4, we discuss the results and we add few concluding remarks.

2. Geometrical principle

2.1. Spatial arrangement

In this section, we introduce a geometrical principle that we exploit to describe the spatial arrangement of the 8-bubbles configuration, to determine the position of the seven bubbles surrounding the central one. The coordinates of the peripheral bubbles centroids are given as solution of the classical *Tammes's Problem* [20]: determine the arrangement of n points on the surface of a sphere maximizing the minimum distance between nearest points (*maxmin principle*). This is equivalent to determine (up to rigid rotations) the n unit vectors $\{\mathbf{r}_i\}$ such that

$$\lim_{m \rightarrow +\infty} \left\{ \frac{1}{|\mathbf{r}_i - \mathbf{r}_j|^m} : 1 \leq i < j \leq n \right\}, \quad (2.1)$$

is maximum, where the limit $m \rightarrow +\infty$ selects the distance among closest points only.

In our case $n = 7$; we want to find the position of seven points on a sphere with minimum distance from their nearest neighbors.

Here, we exploit the *graph theory* [24] to find this maximizing configuration. A set of n points on a sphere forms a graph G of n points connected by arcs of great circles of length a [25]. The maximal spatial arrangement of seven points can be obtained by the projective argument presented in [25].

Consider a frame of reference centered in $O = (0, 0, 0)$ and the coordinates on the spherical surface (r, θ, ϕ) , where $\theta \in [0, 2\pi)$ (longitude) and $\phi \in [0, \pi]$ (latitude) on S^2 , namely

$$S^2 = \{r, 0 \leq \theta < 2\pi, 0 \leq \phi \leq \pi\},$$

where r is the radius of the sphere N and S the North and South Pole, respectively. Three points $\{A, B, C\}$ are placed at the same latitude on the surface of the central sphere, such that they are connected by arcs of length a and they form an equilateral triangle centered in S , see the triangle \widehat{ABC} with in Figure 1a. Three more identical triangles are then created, adjacent to the former ones, with vertices D, E and F : they share the same latitude too, see the triangle \widehat{ABF} in Figure 1b. The final step is then to connect D, E and F with N and vary the radius r (for fixed a) until also the latter arcs have length a^* , (see Figures 1c and 2). The associated extremal graph defines four triangles and three quadrangles on the spherical surface, as illustrated in Figure 3.

*In a fully equivalent way, one can fix the radius r and vary the chord length a .

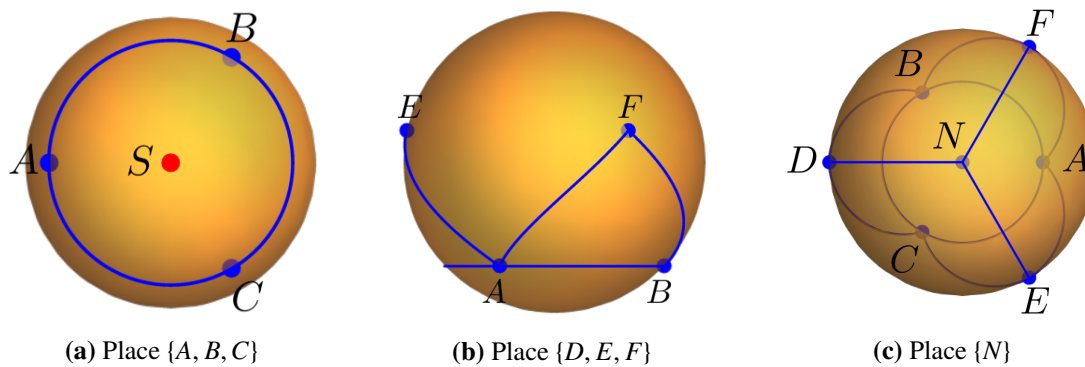


Figure 1. Steps of Tamme's construction. (a) First, we place the three points $\{A, B, C\}$ constructing an equilateral triangle \widehat{ABC} , (b) then we place $\{D, E, F\}$ obtaining three other triangles like \widehat{ABF} , and finally (c) we place the North pole N adapting the radius of the sphere.

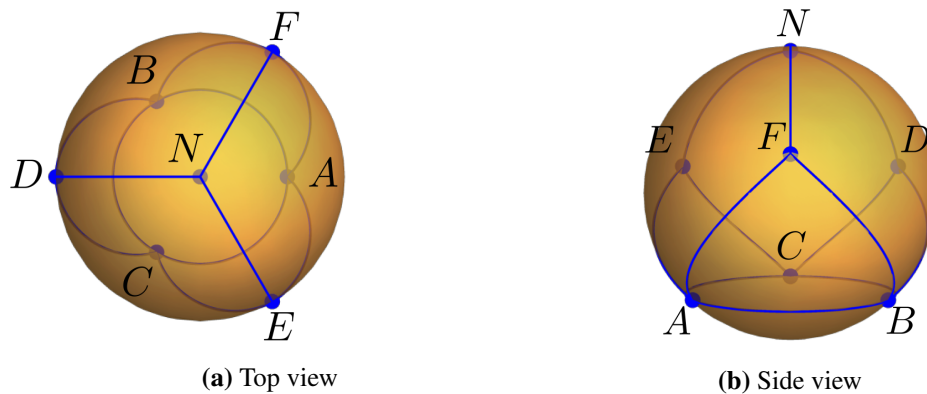


Figure 2. (a) Top and (b) side view of the position and connections of the seven points on the spherical surface of the central bubble. The blue connections are the arcs of length a defined by Tamme's construction.

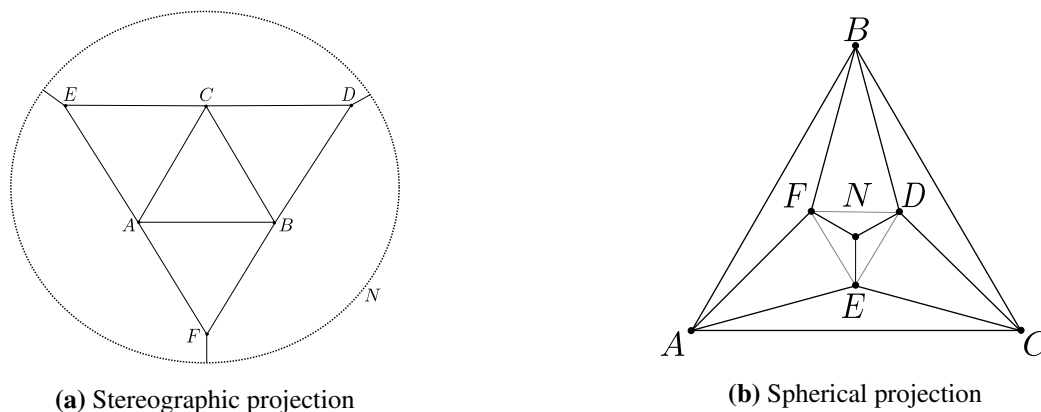


Figure 3. Stereographic (a) and spherical (b) projections of the Tamme's points on the spherical surface and their connecting arcs. Grey and thin lines, corresponding to arcs of length $1.34 a$, making the tessellation fully triangular.

Fundamental relations of spherical trigonometry tell us that the internal angle of an equilateral spherical triangle is $\alpha = \frac{4\pi}{9}$, while the arc angle β with respect to the centre of the sphere β is given by [26]

$$\cos \beta = \frac{\cos \frac{4\pi}{9}}{1 - \cos \frac{4\pi}{9}}, \quad (2.2)$$

as illustrated in Figure 4.

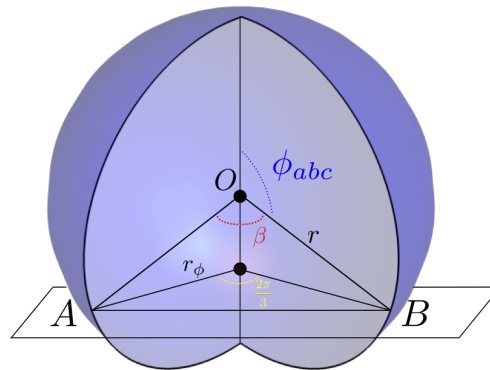


Figure 4. Geometrical sketch of the latitude of the points A , B and C : the central angle β , the radius r of the sphere and the radius r_ϕ of the circumference laying in the plane defined by the triplet of points A , B , C .

This allows to find explicitly the linear relation between arc length and radius, i.e., $a = \beta r$. The length ℓ of the chord between closest points is

$$\ell = 2r \sin\left(\frac{\beta}{2}\right).$$

2.2. Coordinates

By construction, the spherical distance on S^2 of the points D , E and F from N is equal to a , so their latitude is the angle $\phi_{pqr} = \beta$. For the triplet of points $\{A, B, C\}$, the calculations are a little bit more elaborated. Let r_ϕ be the radius of the circumference defined by the intersection of the sphere and the plane where A , B and C are. The following relation holds

$$r_\phi = r \sin(\phi_{abc}), \quad (2.3)$$

where ϕ_{abc} is the latitude of the points A , B and C .

Since the chord length is the same for the spherical arc and for the in-plane circle, we find

$$\frac{\ell}{2} = r_\phi \sin\left(\frac{1}{2} \frac{2\pi}{3}\right) = r \sin\left(\frac{\beta}{2}\right). \quad (2.4)$$

By combining Eqs. (2.3) and (2.4) we get

$$\sin \phi_{abc} = \frac{2}{\sqrt{3}} \sin\left(\frac{\beta}{2}\right). \quad (2.5)$$

Summarizing, the coordinates of the seven Tammes points depicted in Fig. 2 are

$$\begin{aligned} A &= (r, 0, \phi_{abc}) & B &= \left(r, \frac{2\pi}{3}, \phi_{abc}\right) & C &= \left(r, \frac{4\pi}{3}, \phi_{abc}\right), \\ D &= \left(r, \frac{\pi}{3}, \phi_{pqr}\right) & E &= (r, \pi, \phi_{pqr}) & F &= \left(r, \frac{5\pi}{3}, \phi_{pqr}\right) & N &= (r, 0, 0). \end{aligned} \quad (2.6)$$

This configuration, given by the *maxmin principle* (2.1), is here adopted as the ideal reference bubble arrangement: seven spheres are tangent to the former one in the Tammes' points, as illustrated in Figure 5a.

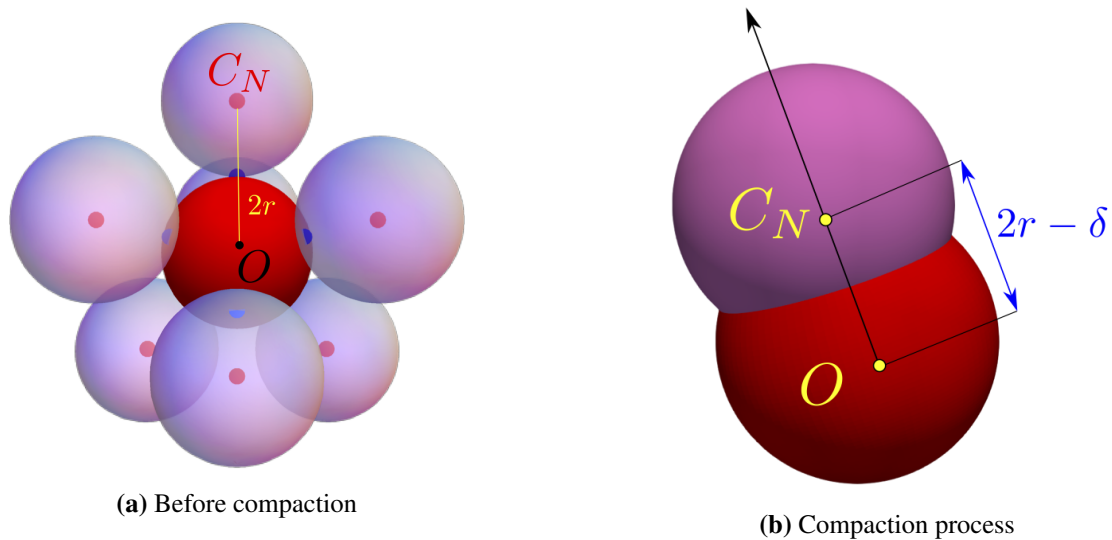


Figure 5. (a) Initial arrangement of the bubbles before compaction. Tangent points are denoted by a blue dot, red dots denote the center of each sphere. (b) Sketch of the “compaction process” between two bubbles driven by the parameter δ .

2.3. “Bubble compaction”: tiling the central sphere

The tessellation of the spherical surface illustrated in the previous sections, is composed by four equilateral triangles and three quadrilaterals, see Figure 3a. However it can be made of triangles only by connecting points $\{D, E, F\}$, see Figure 3b. The triangle $\{D, E, N\}$ is not equilateral, since the distance between D and E is equal to $1.34a$. On the basis of such a triangular tessellation we can produce a *dual* tessellation connecting the circumcenters of the triangles: the locus where the axis of the edges cross each other (Figure 6).

The Tammes' points are the centroids of the polygons that define the dual tessellation (see Figure 6 and for more mathematical details Appendix A). The bubble packing is obtained ideally moving each peripheral bubble, initially tangent to the central one in the Tammes' points, towards the origin O along the radial direction, as illustrated in Figure 5b, while enforcing the volume conservation. In other words, to pack the bubbles aggregate we generate a collection of flat surfaces of contact among bubbles starting from the *maxmin* distribution of the tangent points: each peripheral bubble adheres to the central one moving centripetally, see Figure 5b. At the same time we shuffle the peripheral and the central spheres to preserve the initial volume \mathcal{V} . The contact surfaces between central and

peripheral bubbles obtained by such a *dive and shuffle* procedure are nothing but the polygons obtained connecting the points of the dual tessellation defined above.

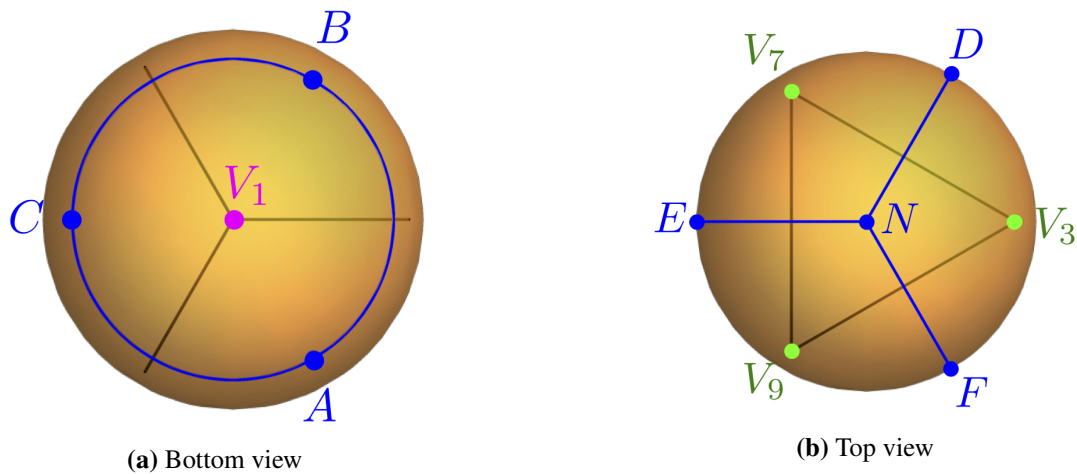


Figure 6. (a) Bottom view of the construction of the dual tessellation. (b) Top view of the construction of the dual tessellation.

The final configuration is a tiling of the spherical surface of the central bubble with seven polygons, as illustrated in Figure 7:

- an equilateral triangle centered in N (area $\simeq 0.66 a^2$),
- three quadrilaterals centered in A, B, C (area $\simeq 0.7 a^2$),
- three pentagons centered in D, E, F (area $\simeq 0.74 a^2$).

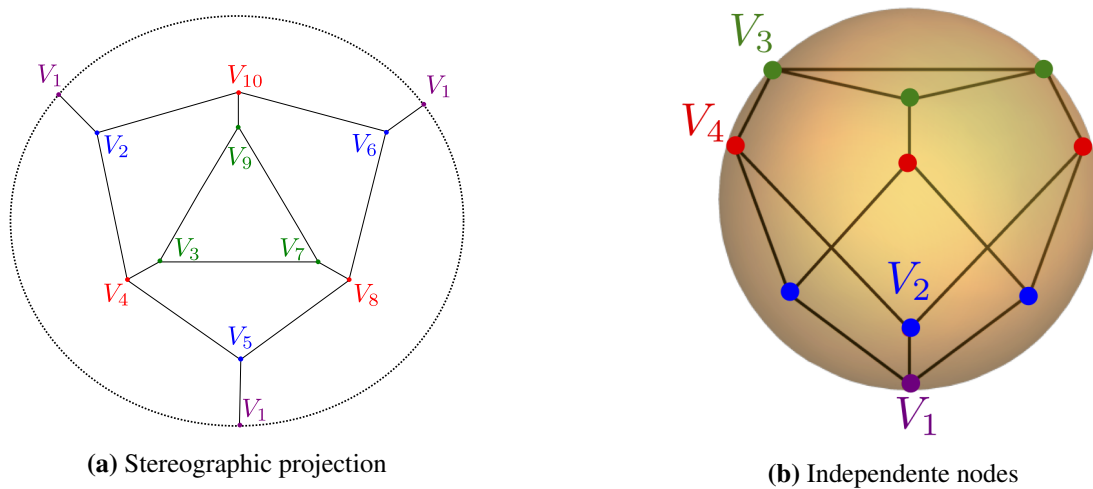


Figure 7. (a) Stereographic projection of the dual tessellation. (b) Sketch of four independent nodes V_1, V_2, V_3 and V_4 on the tessellation, highlighting the corresponding symmetry group.

2.4. Geometrical optimality

While the produced polygonal surface covers the central sphere, it naturally arises the question if such a tiling is optimal according to some suitable criterion. The problem to cover a spherical surface

with polygons is old, rigorous results dating back to Cauchy [27]. In the present context, all the bubbles are identical and it is therefore tempting the idea to cover the central bubble with identical polygons. Unfortunately, this is not allowed by Euler's Polyhedron Formula[†].

There is no regular heptahedron. In order to prove if our tiling is optimal, we can construct all the convex polyhedra with 7 faces which can be inscribed into a sphere of fixed radius r . By the software Plantri [23], we find 34 convex polytopes with seven faces. They can be classified in terms of number of edges and number of vertices, see Table 1.

Table 1. Classification of the 34 convex polytopes with respect to the number of vertices (from left to right) or in terms of edges (from right to left).

Number of vertices	Number of polyhedra	Number of edges
6	2	11
7	8	12
8	11	13
9	8	14
10	5	15

In general, an optimal packing rearrangement of soap bubbles is the one which saves energy, i.e., we expect the chosen one is the equilibrium configuration which should minimize a suitable assigned energy functional. However, due to the huge number of variables involved, we are not able to write down such a functional, hence we use some geometrical and physical considerations to deduce the optimality and maybe the minimality of the obtained configuration.

From a physical point of view, it is known that creating an interface liquid/liquid energetically costs less than one liquid/air [7]. Since the number of edges represents the intersection between nearest bubbles placed on the Tamme's points which creates a liquid/liquid interface, maximizing this number implies that we are requiring that the final polytope on the central sphere has more liquid/liquid intersections than liquid/air ones, i.e., we are looking for a polyhedron \tilde{P} such that

$$\tilde{P} = \max_{E=11}^{15} E_{\mathcal{P}_i} \quad i = 1, \dots, 34, \quad (2.7)$$

where $E_{\mathcal{P}_i}$ is the number of edges the i -polyhedron. In this way, we can reduce the number of polyhedra: we pass from 34 convex polytopes with 7 faces to just 5 in which our tiling is included. In Appendix B, we show these 5 polyhedra obtained and drawn by the software Plantri.

We need another condition to select just one configuration. Using the fact that the shape of a single soap bubble is spherical, which easily derives from the isoperimetric inequality, i.e., the sphere is the only solid that, fixing the area, it maximizes the volume, we search among the five configurations

[†]Euler's Polyhedron Formula has been proved by Cauchy [27] and it gives a relation among the number of faces, edges and vertices of a polyhedron, such as

$$F + V - E = 2.$$

The number of vertices and edges are related with the number of faces F as follows

$$E = \frac{Fn}{2} \quad V = \frac{2E}{m} = \frac{Fn}{m},$$

where n is the number of edges of the polygon at hand, while m is the number of faces which insist on the same vertex. We are interested in the case $F = 7$. By elementary calculations one can easily see that there is no n for which a suitable integer m exists.

obtained by Plantri, the one that has the maximum volume, indeed we look for a polyhedron $\bar{\mathcal{P}}$ such that

$$\bar{\mathcal{P}} = \max_{i=1}^5 (\mathcal{L}^3(\tilde{\mathcal{P}}_i)), \quad (2.8)$$

where \mathcal{L}^3 is the volume measure. By numerically computing the five volumes, we find that the tiling obtained as the dual of the Tammes' one is the one with maximum volume, i.e., the optimal one according to our criteria.

Remark 1. *Since each polyhedron is not regular, we do not have an explicit formula to compute the volume. However, each polyhedron can be divided into 7 pyramids, where the basis is a face. Using this geometrical argument, the total volume can be computed as the sum of the volumes of the pyramids.*

2.5. Surfaces, edges and vertices

The dual tessellation defines ten nodes and it belongs to $C_{3z}(1, 3, 3, 3)$, see Figure 7b[‡]. We denote the nodes of the dual tessellation on the basis of the vertices of the Tammes' triangles they belong to, such as

$$\begin{aligned} V_1 &= (A, B, C), \\ V_2 &= (A, F, B), \quad V_3 = (E, F, N), \quad V_4 = (A, E, F), \\ V_5 &= (A, E, C), \quad V_6 = (B, D, C), \quad V_7 = (D, E, N), \\ V_8 &= (B, D, E), \quad V_9 = (D, F, N), \quad V_{10} = (B, D, F). \end{aligned}$$

Because of the symmetry of the problem, there are only four independent nodes, as depicted in Figure 7b.

The dual tessellation is formed by 15 edges, only 4 of them being independent. Each edge is identified by the polygons it belongs to on the tiled surface and the boldface denotes the unit vector parallel to the edge. Therefore, $\mathbf{c}_1 = \overline{V_1 V_2}$ denotes the edge between two quadrilaterals, $\mathbf{c}_2 = \overline{V_2 V_3}$ separates a quadrilateral and a pentagon, $\mathbf{c}_3 = \overline{V_3 V_4}$ separates a pentagon and a pentagon and $\mathbf{c}_4 = \overline{V_2 V_3}$ is between a pentagon and the triangle.

We generate a three dimensional structure projecting radially the dual tessellation, by an height to be fixed later on the basis of volume conservation arguments. Each vertex of the tessellation on the central bubble has therefore a corresponding outer one that we denote by V_i^h , $i = 1, 2, 3, 4$. The connection between inner, outer and side surfaces is defined by two classes of edges:

- $\mathbf{c}_5 = \overline{V_1 V_1^h}$, $\mathbf{c}_6 = \overline{V_2 V_2^h}$, $\mathbf{c}_7 = \overline{V_3 V_3^h}$, $\mathbf{c}_8 = \overline{V_4 V_4^h}$ point radially,
- $\mathbf{c}_9 = \overline{V_1^h V_2^h}$, $\mathbf{c}_{10} = \overline{V_2^h V_3^h}$, $\mathbf{c}_{11} = \overline{V_3^h V_4^h}$, $\mathbf{c}_{12} = \overline{V_2^h V_3^h}$, are parallel to the ones on the tessellation of the central bubble.

At this stage the geometrical characterization of the 8-bubbles configuration derived on the basis of a maximum-minimum distance of the centroids of the peripheral bubbles is completed. The inner bubble has no free surface: it is surrounded by contact interfaces with other bubbles only. The external ones have the shape of a pyramidal frustum covered by a laterally cut spherical cap: the lower basis is the polygon generated by the adhesion with the central bubble, lateral sides are flat too, their edges being

[‡] C_{nz} is the group of a cyclic symmetry after a rotation $2\pi/n$ with respect to the axis z [28, 29]: the configuration is invariant for rotations of an angle $2\pi/3$ around the z axis. The notation $(1, 3, 3, 3)$ denotes how many nodes of the tessellation share the same longitude.

radially oriented, the upper basis of the frustum is a radial projection of the lower one. The upper geometrical structure is a spherical vault on a polygonal frustum, intriguingly known since the Middle Age in Sicilian architecture [30]. The radius of the spherical cap and the height of the frustum are to specified on the basis of balance and conservation arguments discussed below.

3. Mechanical balance

In this section, we compute the surface tensions that make the geometrical packing mechanically equilibrated. We remark that the central sphere has only bubble–bubble contact interfaces, while the peripheral ones also possess a traction–free surface. Each bubble–bubble interface and each free surface is characterized by a tension τ_i , defined as the energy density per unit area of the liquid/liquid or liquid/air interfaces [31]. Thus, for the strong symmetry of the problem, we have ten unknown independent tensions τ_i , one variable for each portion of surface. Precisely, they are: three on the central bubble, four on lateral bubble-bubble interfaces and three at the free surface denoted by

$$\tau_Q, \tau_P, \tau_T, \tau_{QQ}, \tau_{PQ}, \tau_{PP}, \tau_{PT}, \tau_Q^s, \tau_P^s, \tau_T^s, \quad (3.1)$$

where the subscript identifies the surface of the polygon it applies to and the superscript s specifies the tensions at the free surfaces.

3.1. Tensional balance

First, we enforce the mechanical equilibrium imposing that the surface tensions are balanced on each independent edge \mathbf{c}_i , where $i = 1, \dots, 12$ (see Figure 8a). Three (flat or curved) surfaces are attached to each edge, their local orientation being denoted by the normal unit vectors \mathbf{n}_j^i , $j = 1, 2, 3$. The balance of tensions on each edge is defined by the sum of the tensions, oriented orthogonally to the edge and in-plane with the corresponding interface (see Figure 8a). Therefore it must hold

$$\sum_{j=1}^3 \mathbf{t}_j \tau_j = \sum_{j=1}^3 \mathbf{c}_i \times \mathbf{n}_j^i \tau_j = \mathbf{c}_i \times \sum_{j=1}^3 \mathbf{n}_j^i \tau_j = 0 \quad \Rightarrow \quad \sum_{j=1}^3 \mathbf{n}_j^i \tau_j = 0 \quad i = 1, \dots, 12 \quad (3.2)$$

Equation (3.2) defines 36 scalar equations, 12 of them being trivially null because all the summed vectors are in the plane orthogonal to the edge under consideration. With the help of a symbolic software[§], we eventually find that, given the unit vectors \mathbf{n}_j^i only 10 of them are independent[¶]. The equations are detailed in Appendix D in Tables 2–4.

The linear system Eq (3.2) is however not closed because, while the direction orthogonal to the flat surfaces is uniquely defined, the edge contribution of the tension defined on the free surface depends on the curvature of the surface itself. Curvature, tension and pressure gap on the free surface of the peripheral bubbles obey the Young-Laplace equation [32] in the following way

$$\Delta p = \frac{4\tau_i^s}{R_i} \quad i = P, Q, T, \quad (3.3)$$

[§]We used Mathematica (Wolfram Inc., Version 12).

[¶]The orientation of the normal unit vectors is not defined according any specific rule because it is expected to affect only the sign of tension, that we know to be positive.

where R_i is the radius of curvature of the free surface of the i -th bubble and Δp is the difference between the outer and the inner of pressure and there is an extra factor 2 since the surface of the bubble is composed by two leaflets. Since we have only three independent types of polygons on the tessellation, Eq (3.3) gives three independent equations.

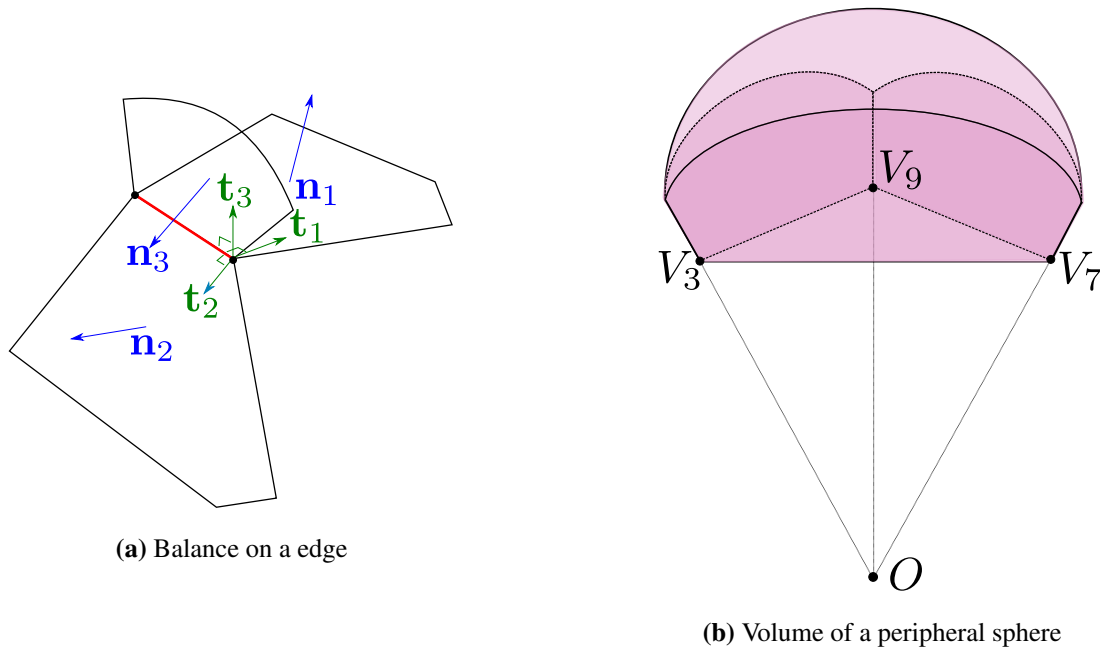


Figure 8. (a) Balance of tensions on an edge. (b) The bubble volume is the sum of a pyramidal frustum (with pink side boundaries) plus the polygonal–basis vault standing on it (light pink).

3.2. Volume conservation

Finally, we have to impose the conservation of bubble volume under compaction. While the central (packed) bubble is bounded by flat interfaces, the peripheral ones have the shape of a pyramidal frustum covered with a spherical vault (see Figure 8b). The basis of the pyramidal frustum are

- the interface with the central bubble;
- its radially directed homothetic projection, by a factor $\frac{r+h}{r}$, where h is the radial height of the intersection surface among three adjacent cells (see the yellow segment in Figure 9).

The value of h has to be fixed on the basis of volume conservation arguments: the sum of the pyramidal and apsal volumes must be equal to the common volume of all bubbles.

Details about the calculation of these volumes are given in Appendix C. As the area of each polygonal basis and the curvature radius of the apse are different, the radial height h of the cells is not actually the same; however differences are below 1%.

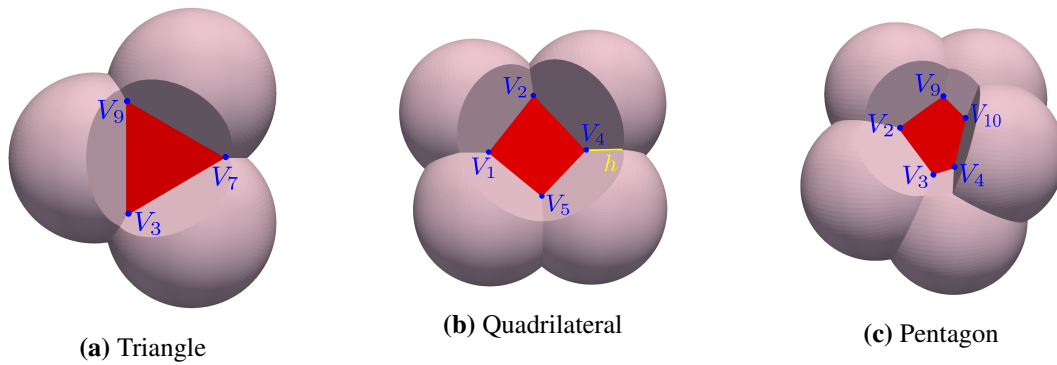


Figure 9. Compactification of peripheral bubbles around (a) the triangle, (b) a quadrilateral and (c) a pentagon. The corresponding peripheral bubble is removed for the sake of graphical representation. The yellow segment represents the radial height h of the intersection surface among three adjacent bubbles.

3.3. Results

We can solve the system of 16 equations given by Eqs (3.2) and (3.3), constrained to volume conservation, with respect the 16 unknowns: 10 tensions, 3 curvature radii and 3 heights. Using some experimental data coming from the foam literature, [22], we can fix the pressure difference $\Delta p = 50$ Pa and the radius of the round bubble as $r = 1$ mm, before the compaction process. Numerical solution of the nonlinear system of equations predicts the following surface tensions

$$\begin{cases} \tau_P = 51 \frac{mN}{m} & \tau_T = 45 \frac{mN}{m} & \tau_Q = 47 \frac{mN}{m} \\ \tau_{PP} = 69 \frac{mN}{m} & \tau_{QQ} = 58 \frac{mN}{m} & \tau_{PT} = 63 \frac{mN}{m} & \tau_{PQ} = 65 \frac{mN}{m} \\ \tau_P^s = 41 \frac{mN}{m} & \tau_T^s = 35 \frac{mN}{m} & \tau_Q^s = 39 \frac{mN}{m}. \end{cases} \quad (3.4)$$

The computed radii of curvature are

$$R_P = 3.5 \text{ mm}, \quad R_T = 2.5 \text{ mm}, \quad R_Q = 3.1 \text{ mm}. \quad (3.5)$$

The obtained surface tensions are consistent with experimental results [22]: to create a soap bubble, the surface tension has to be less than the one of water, which is $\tau_{\text{water}} \approx 73 \text{ mN/m}$, otherwise the bubble cannot exist. The obtained field of forces Eq (3.4) is the one at the equilibrium. We immediately notice that there is an anisotropy in the distribution of the field of forces: surface tensions of bubble-bubble interfaces with normal oriented in the circumferential direction of bubbles aggregate (second line of Eq (3.4)) are larger than the ones with normal unit vector pointing radially out of the aggregate (first and third line of Eq (3.4)).

This result supports our conjecture: the anisotropy in the mechanical cues may be the cause of the symmetry break, i.e., there might be a preferential direction of the next topological instability [13]. Indeed, from experiments and numerical results, it is known that a similar aggregate, due to some physical involved parameters, can develop an asymmetry or a topological transition [15]. The study of the stability of this configuration is out of this paper. This result wants just to show that the distribution

of forces in the equilibrium configuration itself is not symmetric, hence we can state that any small perturbations can change the rearrangement of forces inside the system and can develop a topological transition which breaks the starting symmetrical structure.

4. Final remarks

In this work, we studied the symmetry break of a particular configuration of 8 spheres, showing the anisotropy in the distribution of the field of forces of the equilibrium position, that might possible originate a topological transition and break the symmetric structure of the starting agglomerate [13, 15]. This result can be applied to a physical situation, i.e., the study of foam, since the selected rearrangement remembers the one of soap bubbles in a single module of the foam structure [22].

We considered 7 identical spheres symmetrically surrounding a central one: their initial position is dictated by the solution of the Tammes' problem [20]. Neglecting any dynamical process, the final configuration is obtained by a compaction process which results into a full tiling of the central sphere. By introducing physical criteria of optimality dictated by the energy minimality, Eq (2.7), and by the volume maximality, Eq (2.8), we deduced that our polyhedra is the optimal one among all the 34 convex polytopes inscribed into a sphere with radius r [23], since due to Euler Polyhedra Formula no regular heptahedrons exist [27].

Fixing this geometrical arrangement, we looked for the force balance that realizes such a configuration: we computed balance of forces on every edge, we forced the conservation of volume (by experimental evidences soap bubbles can be assumed to be incompressible [33]) and we imposed the Laplace law on the possibly curved free surface. We obtained a force field, Eq (3.4), which fulfills an acceptable physical range [22], but it shows an anisotropy in its orientation, see second line in Eq (3.4). This result suggests that a difference in tension, generated by a purely mechanical principle, might be crucial for next topological transitions and for the development of anisotropies [15]. In this respect, we conjecture that the expulsion of a single bubble, dictated by any small perturbations, in the *flower cluster* in 2D [13] can be replicated in higher dimensions, breaking the symmetrical structure. Indeed, our configuration represents a 3D asymmetrical flower cluster. Hence, up to construct a suitable dynamical problem to study the evolution in time of such a configuration, a possible solution might be the ejection of one bubble from the agglomerate.

Future efforts will be devoted first to try to understand more rigorously if the obtained dual tessellation realizes the minimum of a suitable energy functional, then to reproduce this system both in a laboratory and numerically to study the dynamical evolution of this agglomerate.

The main novelty of this work is the introduction of a new non-destructive technique to study the geometrical rearrangement and the change of shape of a configuration by using mechanical and geometrical considerations. Indeed, the used mathematical method here is applied to a specific context, i.e., the symmetry break of a 8-bubble compaction, but it can be extended to better understand many different physical phenomena. For instance, it can be used to design new meta-materials, where it is fundamental to know a priori the balance of forces, or to study the mitosis of cells. Indeed, just by knowing their geometrical rearrangement at a fixed stage, we can determine if the distribution of forces has an anisotropy which can favour the duplication process along a particular direction [34]. This means that our method can give an insight for a more detail comprehension on the mechanics of morphogenesis of a variety of tissues.

Acknowledgments

The author thanks Davide Ambrosi, Pasquale Ciarletta, Luca Lussardi, Alfredo Marzocchi and Maurizio Paolini for helpful suggestions and fruitful discussions. This work has been partially supported by INdAM–GNFM.

Conflict of interest

The author declares no conflict of interest.

References

1. J. P. Plateau, Recherches expérimentales et théorique sur les figures l'équilibre d'une masse liquide sans pesanteur, *Mémoires de l'Académie Royale des Sciences, des Lettres et des Beaux-Arts de Belgique*, **37** (1869), 1–56.
2. H. Kellay, W. I. Goldburg, Two-dimensional turbulence: a review of some recent experiments, *Rep. Prog. Phys.*, **65** (2002), 845.
3. P. Morel, M. Larceveque, Relative dispersion of constant-level balloons in the 200-mb general circulation, *J. Atmos. Sci.*, **31** (1974), 2189–2196.
4. T. Meuel, Y. L. Xiong, P. Fischer, C. H. Bruneau, M. Bessafi, H. Kellay, Intensity of vortices: from soap bubbles to hurricanes, *Sci. Rep.*, **3** (2013), 1–7.
5. F. Seychelles, Y. Amarouchene, M. Bessafi, H. Kellay, Thermal convection and emergence of isolated vortices in soap bubbles, *Phys. Rev. Lett.*, **100** (2008), 144501.
6. J. J. Bikerman, Formation and structure, In: *Foams*, Springer, 1973, 33–64.
7. D. L. Weaire, S. Hutzler, *The physics of foams*, Oxford University Press, 2001.
8. T. C. Hales, The honeycomb conjecture, *Discrete Comput. Geom.*, **25** (2001), 1–22.
9. F. J. Almgren Jr., Existence and regularity almost everywhere of solutions to elliptic variational problems with constraints, *Mem. Am. Math. Soc.*, **5** (1976), 165.
10. F. Morgan, Geometric measure theory, In: *Geometric measure theory: a beginner's guide*, Elsevier, 2016, 3–15.
11. S. J. Cox, F. Graner, F. Vaz, C. Monnereau-Pittet, N. Pittet, Minimal perimeter for N identical bubbles in two dimensions: calculations and simulations, *Philos. Mag.*, **83** (2003), 1393–1406.
12. K. A. Brakke, F. Morgan, Instabilities of cylindrical bubble clusters, *Eur. Phys. J. E*, **9** (2002), 453–460.
13. S. J. Cox, M. F. Vaz, D. Weaire, Topological changes in a two-dimensional foam cluster, *Eur. Phys. J. E*, **11** (2003), 29–35.
14. M. A. Fortes, M. F. Vaz, S. J. Cox, P. I. C. Teixeira, Instabilities in two-dimensional flower and chain clusters of bubbles, *Colloid. Surface. A*, **309** (2007), 64–70.
15. D. Weaire, M. F. Vaz, P. I. C. Teixeira, M. A. Fortes, Instabilities in liquid foams, *Soft Matter*, **3** (2007), 47–57.

16. A. C. Ferro, M. A. Fortes, The elimination of grains and grain boundaries in grain growth, *Interface Science*, **5** (1997), 263–278.
17. M. Hutchings, F. Morgan, M. Ritoré, A. Ros, Proof of the double bubble conjecture, *Ann. Math.*, **155** (2002), 459–489.
18. W. Thomson, On the division of space with minimum partitional area, *The London, Edinburgh, and Dublin Philosophical Magazine and Journal of Science*, **24** (1887), 503–514.
19. D. Weaire, R. Phelan, A counter-example to Kelvin’s conjecture on minimal surfaces, *Phil. Mag. Lett.*, **69** (1994), 107–110.
20. P. M. L. Tammes, On the origin of number and arrangement of the places of exit on the surface of pollen-grains, *Recueil des Travaux Botaniques Néerlandais*, **27** (1930), 1–84.
21. T. W. Melnyk, O. Knop, W. R. Smith, Extremal arrangements of points and unit charges on a sphere: equilibrium configurations revisited, *Can. J. Chem.*, **55** (1977), 1745–1761.
22. I. Cantat, I. S. Cohen-Addad, F. Elias, F. Graner, R. Höhler, O. Pitois, et al., *Foams: structure and dynamics*, OUP Oxford, 2013.
23. G. Brinkmann, B. D. McKay, Fast generation of planar graphs, *MATCH Commun. Math. Comput. Chem.*, **58** (2007), 323–357.
24. D. B. West, *Introduction to graph theory*, Prentice hall Upper Saddle River, 2001.
25. K. Schütte, B. L. Van der Waerden, Auf welcher Kugel haben 5, 6, 7, 8 oder 9 Punkte mit Mindestabstand eins Platz?, *Math. Ann.*, **123** (1951), 96–124.
26. M. Berger, *Geometry revealed: a Jacob’s ladder to modern higher geometry*, Springer Science & Business Media, 2010.
27. A. L. Cauchy, Recherches sur les polyedres, *J. Ecole Polytechnique*, **9** (1813), 68–86.
28. B. W. Clare, D. L. Kepert, The closest packing of equal circles on a sphere, *Proc. R. Soc. Lond. A*, **405** (1986), 329–344.
29. D. E. Sands, *Introduction to crystallography*, Courier Corporation, 1993.
30. E. Garofalo, Absidi poligonali e impianti basilicali della Sicilia tardo-medievale, In: *L’abside, costruzione e geometrie*, 2015, 169–185.
31. B. Roman, J. Bico, Elasto-capillarity: deforming an elastic structure with a liquid droplet, *J. Phys. Condens. Mat.*, **22** (2010), 493101.
32. G. K. Batchelor, *An introduction to fluid dynamics*, Cambridge university press, 2000.
33. D. Exerowa, P. M. Kruglyakov, *Foam and foam films: theory, experiment, application*, Elsevier, 1997.
34. E. Korotkevich, R. Niwayama, A. Courtois, S. Friese, N. Berger, F. Buchholz, et al., The apical domain is required and sufficient for the first lineage segregation in the mouse embryo, *Dev. Cell*, **40** (2017), 235–247.

Appendix A Dual tessellation of the central bubble

A visual three-dimensional representation of the dual tessellation produced on the central sphere by the bubble packing is depicted in Figures 10 and 11. The polygons representing the flat bubble–bubble interfaces are here plotted inside the original spherical bubble of radius r before reshuffling the polyhedron to recover the original bubble volume.

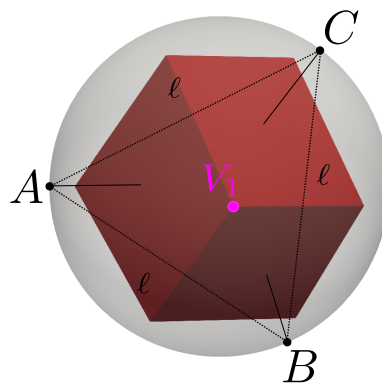


Figure 10. Bottom view of the dual tessellation. The dashed lines represent the chord ℓ of the Tamme's construction. The centroid of the triangle A, B, C is the South Pole, called V_1 in the dual tessellation.

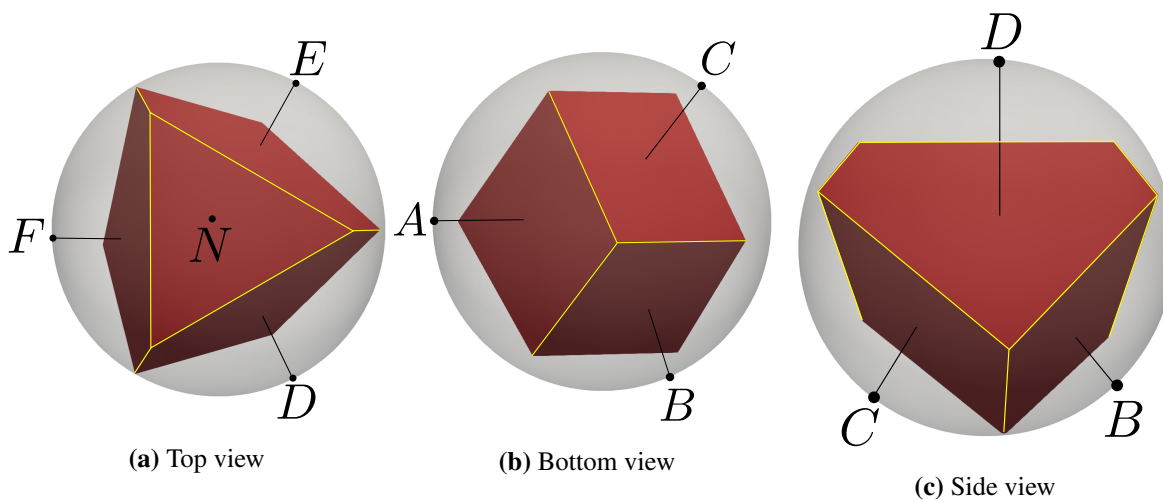


Figure 11. Different views of the tessellation: (a) top, (b) bottom and (c) side view. Black dots indicate the Tamme's points. Irrespective of the graphic illusion, the corners of the inscribed polyhedron are on the spherical surface; after restoring of the initial volume, they will be external. Yellow lines underline the sides of the different obtained polygons: (a) a triangle, (b) three quadrilaterals and (c) three pentagons.

As we can see from Figures 10 and 11, the projection of Tamme's points along the radial direction represents the centroid of each polygon on the dual tessellation. Viceversa, the vertices V_i with $i = 1, \dots, 10$ are the centroids of the triangles of the modified Tamme's tessellation, see Figure 3b.

Appendix B Polyhedra with seven faces

In this appendix, we want to show the five polyhedra among all the 34 convex polytopes with seven faces inscribed into a sphere of a fixed radius r , which satisfies the first optimal criterium, i.e., Eq (2.7). By the software Plantri, we can draw them and their graphical representation is presented in Figure 12.

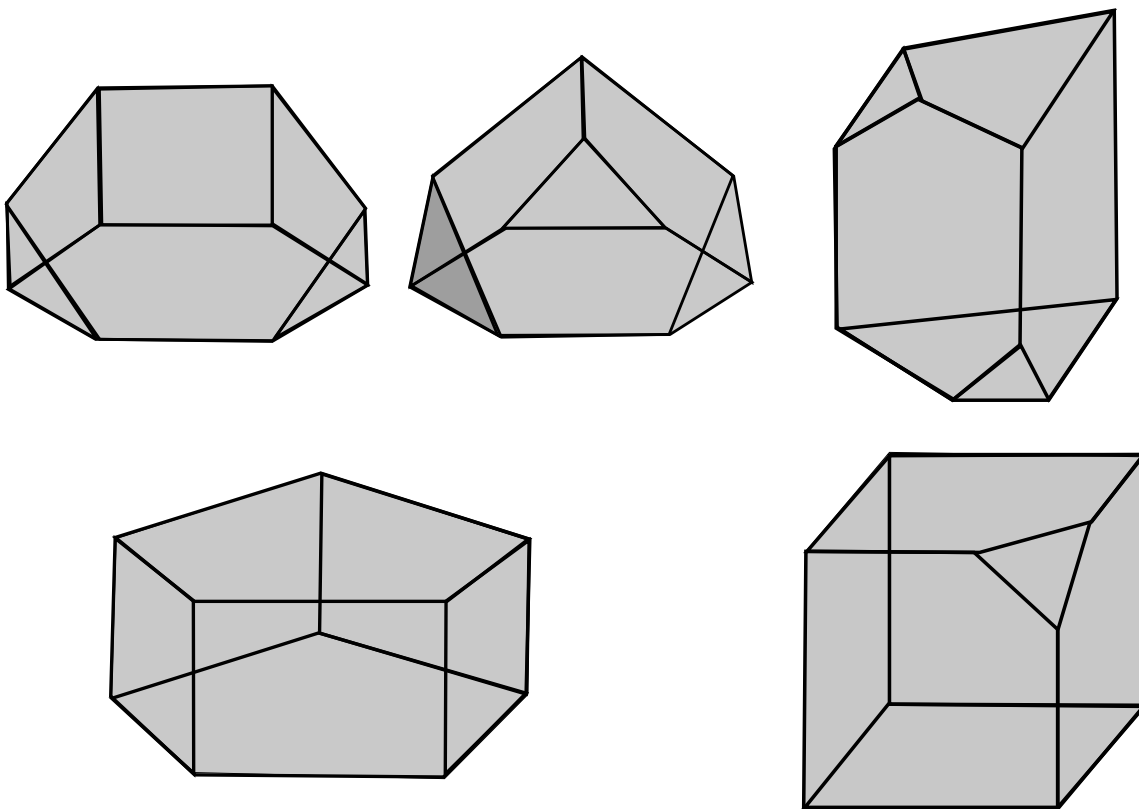


Figure 12. Graphical representation, obtained through the software Plantri, of the five convex polyhedra among the 34 inscribed into a sphere which satisfy the first optimal criterium Eq (2.7). The Tamme's dual tessellation is one of them, i.e., the last one.

Appendix C Calculation of volumes

In order to compute the volume of the peripheral bubbles, we have to mathematically describe the shape of a pyramidal frustum covered by a vault. The vault is obtained radially cutting slices of a spherical cap drawn on the vertices of the external basis of the frustum, by prolongation of the lateral surfaces of the frustum itself (see Figures 8b and 14a). From a mathematical point of view, this calculation is a bit technical since the final solid is not a known or a common one.

First of all, we have to better clarify which are the involved unknowns. As it concerns the packing parameter, which is used to define the position of the vertices on the free surface and it is obtained through the interaction among three surfaces, we a priori have four different values of packing

parameter, i.e.,

$$h_1 = h(Q, Q, Q) \quad h_2 = h(P, P, T) \quad h_3 = h(Q, P, Q) \quad h_4 = h(Q, P, P), \quad (C.1)$$

where the letters into brackets denote the interaction between three polygons, i.e., P for pentagons, Q for quadrilaterals and T for the triangle.

We denote with the symbol $\tilde{}$ the centroids of the dual tessellation polygon: $\tilde{A}, \tilde{B}, \tilde{C}, \dots$, and with C_i , with $i = A, B, C, D, E, F, N$, the center of the sphere passing through the vertices of the homotetically projected polygons. Since we have three type of polygons, we make the calculations only on a representative of each class, such as on the quadrilateral A , on the pentagon D and on the triangle N . We define $h_P = \tilde{D} - C_D$, $h_Q = \tilde{A} - C_A$ and $h_T = \tilde{N} - C_N$ (see Figure 13) the distance between the centre of the sphere associated with the vault curvature and the centroid of the polygonal inner basis of the frustum (the projection of the Tammes' points on the central bubble interfaces). These distances have to be fixed in order to enforce conservation of volumes of the peripheral bubbles. Depending on the type of adjacent polygons (pentagon-pentagon, pentagon-triangle,...), a different packing parameter h_i with $i = 1, 2, 3, 4$ is expected (see Eq (C.1)). For illustrative purposes, here below we only show how the radial height h_2 , obtained by the intersection among the sphere constructed on the triangle and on the two adjacent pentagons. We are going to show that it can be rewritten as a function of h_P (Figure 13).

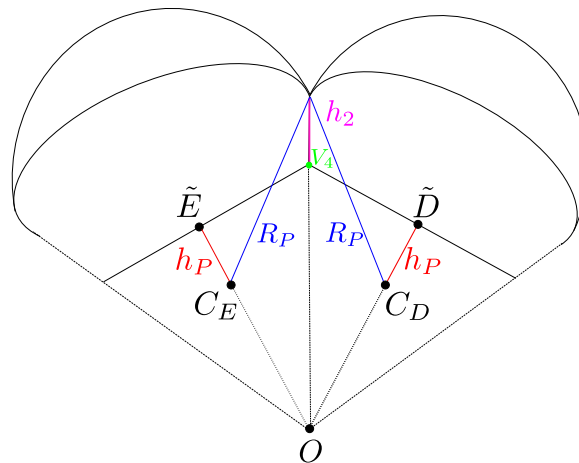


Figure 13. In the plane passing through the projected Tammes points \tilde{D} , \tilde{E} and the origin O , the points C_D and C_E are the centres of the spheres of radius R_P , that eventually define the free surface of the bubble. The side of the pyramidal frustum is h_2 .

The sphere of radius R_P , centered in C_D is defined by the equation

$$(x - x_{C_D})^2 + (y - y_{C_D})^2 + (z - z_{C_D})^2 = R_P^2, \quad (C.2)$$

where the coordinates of C_D are

$$C_D = (d x_{\tilde{D}}, d y_{\tilde{D}}, d z_{\tilde{D}}) \quad \text{with} \quad d = 1 - \frac{h_P}{r}.$$

Analogously, we construct the sphere on the adjacent pentagon E , so that

$$(x - x_{C_E})^2 + (y - y_{C_E})^2 + (z - z_{C_E})^2 = R_P^2. \quad (C.3)$$

The same compation parameter d scales the coordinates $(x_{C_E}, y_{C_E}, z_{C_E})$ because both D and E are pentagons.

The intersection between the two spheres is a circumference, and the edge $\mathbf{c}_3 = \overline{V_3V_4}$ lies on it. In the same way, we can also consider another circumference obtained by the intersection of, for instance, the sphere centered in C_D and the adjacent constructed on the triangle, i.e., centered in C_N . The length of the side of the frustum h_2 is the distance between the node V_4 of the dual tessellation and the outer intersection point of the two circumferences defined above. The parametric representation of the radial line passing through $V_4 = (x_{V_4}, y_{V_4}, z_{V_4})$ is given by

$$\begin{cases} x = tx_{V_4}, \\ y = ty_{V_4}, \\ z = tz_{V_4}, \end{cases} \quad (\text{C.4})$$

where t is a positive real parameter. The intersection between the two spherical surfaces Eqs (C.2) and (C.3) with the line Eq (C.4) is the point \mathbf{x}_0 on the free surface with the following coordinates (where $z_{V_4} \neq 0$ by construction)

$$\mathbf{x}_0 : \begin{cases} x = \frac{x_{V_4}}{z_{V_4}}z \\ y = \frac{y_{V_4}}{z_{V_4}}z \\ z = \frac{(-x_{C_P}^2 + x_{C_Q}^2 - y_{C_P}^2 + y_{C_Q}^2 - z_{C_P}^2 + z_{C_Q}^2)z_{V_4}}{-2(x_{C_P} + x_{C_Q})x_{V_4} - 2(y_{C_P} + y_{C_Q})y_{V_4} - 2(z_{C_P} + z_{C_Q})z_{V_4}}. \end{cases} \quad (\text{C.5})$$

Hence, we define

$$h_2 = |\mathbf{x}_0 - V_4|. \quad (\text{C.6})$$

This procedure can be repeated on all the lateral interfaces in order to calculate all the h_i with $i = 1, 2, 3, 4$.

The second and final step is to write down the volume of the solid (pyramidal frustum plus spherical vault) as a function of h_P , h_T and h_Q calculated as in Eq (C.5). The volume of the pyramidal frustum is

$$\mathcal{V}_{\text{py}}^i = \frac{\left(A_{\text{bottom}}^i + A_{\text{top}}^i + \sqrt{A_{\text{bottom}}^i A_{\text{top}}^i}\right) H_{\text{py}}^i}{3} \quad i = P, Q, T, \quad (\text{C.7})$$

where A_{bottom}^i is the area of the i -th polygon on the dual tessellation, $A_{\text{top}}^i = \frac{r+h}{r}A_{\text{bottom}}^i$ is the area of the upper basis, and H_{py}^i is the height of the pyramidal frustum.

The volume of the spherical vault is nothing but the volume of the laterally cut spherical cap. For the sake of simplicity, we consider here the spherical vault based on the triangle N . We use local coordinates with origin in C_N , the centroid of the triangle is in $\tilde{N} = (0, 0, h_T)$.

In terms of the local coordinates (x', y', z') , the volume of the spherical cap is

$$\Omega' = \{(x', y', z') \in \mathbb{R}^3 : (x')^2 + (y')^2 + (z')^2 \leq R_T^2, z' \geq h + h_T\}.$$

and its measure is obtained by standard volume integration. We have to subtract to the measure of Ω' the volume of the slices obtained by prolongation of the flat interface defined by the vertices V_3V_7

(and so on). It is worth to remark that the plane attached to V_3V_7 is not perpendicular to basis of the spherical cap. So, first of all, the expression of the area of a circular segment of radius ρ and chord b is

$$\mathcal{A}_{cir} = \rho^2 \left(\arcsin \left(\frac{b}{2\rho} \right) - \frac{b}{2\rho} \right). \quad (\text{C.8})$$

Here ρ and b are functions of the quote $z' \in [h + h_T, h_{\max}]$ and h_{\max} has to be determined, see Figure 14a. The value of h_{\max} is fixed at the z' -level such that the homothetic projection of the inner triangle is circumscribed into the circumference. Namely, a plane at given z' crosses the plane defined by V_3V_7 along a line, that we represent by its equation $ax' + by' + c = 0$. To obtain the upper integration bounds in z' we impose

$$\frac{|a\bar{x}' + b\bar{y}' + c|}{\sqrt{a^2 + b^2}} = \sqrt{R_T^2 - (z')^2}, \quad (\text{C.9})$$

where $\bar{x}' = 0$, $\bar{y}' = 0$ and the left-hand-side of Eq (C.9) is exactly the radius ρ of the circumference at fixed z' .

By solving (C.9), we get

$$z'_{1,2} = \frac{-cd \pm \sqrt{c^2d^2 - (a^2 + b^2 + c^2)(d^2 - R_T^2a^2 - R_T^2b^2)}}{c^2 + a^2 + b^2},$$

where $a = 2.48 - 2.96h_T$, $b = 0$, $c = 1$ and $d = 0.42 - h_T$ and h_{\max} is the positive value, since it belongs to Ω' .

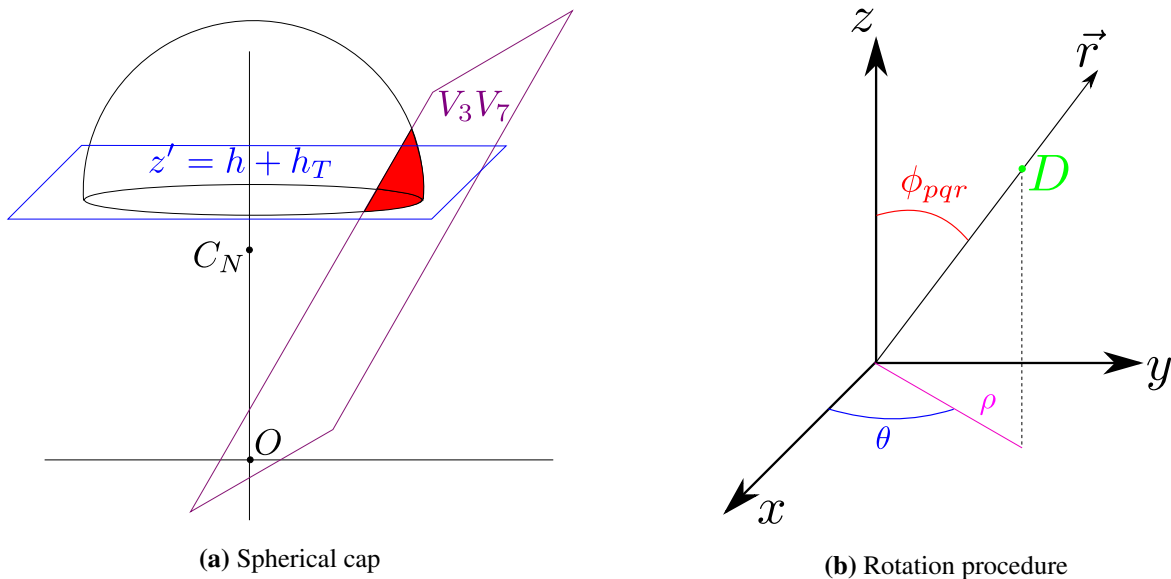


Figure 14. (a) Geometrical representation of the lateral cut of the spherical cap. (b) Geometrical sketch of the rotation around the axis x by the angle ϕ_{pqr} . The coordinates ρ , θ and ϕ are the spherical ones set into a Cartesian frame of reference (x, y, z) .

Finally, the volume of the bubble constructed on the triangle is given by

$$\mathcal{V}_T = |\Omega'| - 3 \int_{h+h_T}^{h_{\max}} \mathcal{A}_{cir} d\alpha,$$

where $|\cdot|$ denotes the measure of the volume of Ω' . All the calculations are computed numerically by using the Newton's method with the software *Mathematica* 12 (Wolfram Research, Champaign, IL, USA). For the other polygons, the computation is similar up to a rotation which has to be done before computing the translation of the centre of the frame of reference, see Figure 14b.

Appendix D Equations of balance of tensions

The detailed expressions of Eq (3.2) and their geometrical representation are listed in Tables 2–4. We introduce different superscripts to distinguish the different directions. The unit vectors denoting the direction of the force on the side edge is denoted by the symbol \mathbf{t} , \mathbf{t}^r for the ones oriented in the radial direction, \mathbf{t}^s on the free surface.

In the following tables, the unit vector normal to the free surface applied in the homothetical vertex of the dual Tamme's tessellation are not reported due to absence of space. We collect them below, i.e.,

$$\begin{aligned}\mathbf{n}_D^s &= (-0.18 + 0.39h_2 + 0.62h_P, 0.53 + 0.68h_2, -0.4 - 0.64h_2 - 0.13h_P) \\ \mathbf{n}_E^s &= (0.55 + 0.39h_2 - 0.3h_P, 0.11 + 0.67h_2 + 0.58h_P, -0.4 - 0.64h_2 - 0.13h_P) \\ \mathbf{n}_A^s &= (0.48 + 0.83h_4 + 0.23h_Q, -0.31 + 0.3h_Q, 0.11 + 0.56h_4 + 0.43h_Q) \\ \mathbf{n}_B^s &= (0.35 - 0.44h_Q, 0, 0.46 + h_4 + 0.43h_Q) \\ \mathbf{n}_N^s &= (0.31 + 0.39h_3, -0.53 - 0.67h_3, -0.09 - 0.64h_3 - 0.53h_T),\end{aligned}$$

where h_P , h_Q and h_T are the distance between the center of the sphere associated with the vault curvature and the centroid of the polygonal inner basis of the frustum, for more details see Appendix C.

Table 2. Edges on the tessellation.

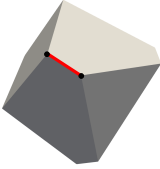
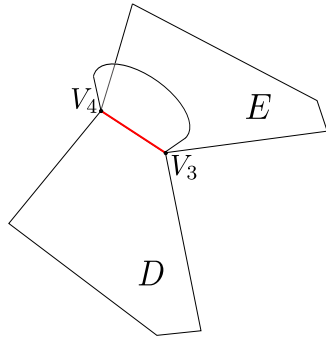
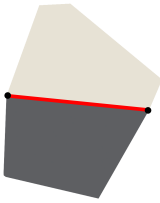
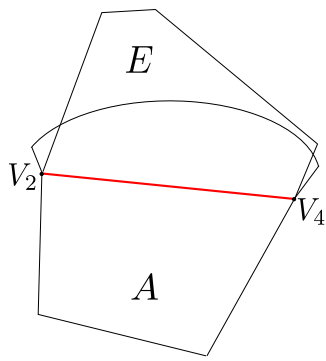
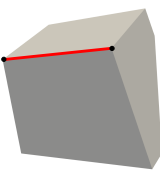
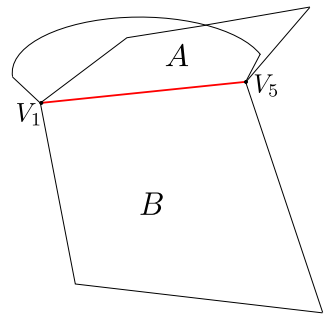
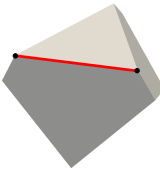
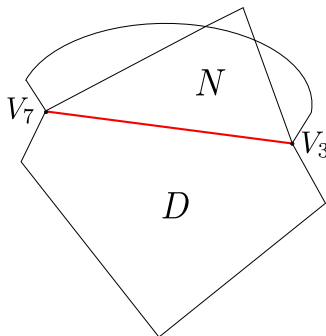
Adjacent polygons	Edges	Vectors	Equation
pentagon–pentagon 		$V_3 = (-0.3, -0.53, 0.51)$ $V_4 = (-0.38, -0.66, 0.2)$ $\mathbf{n}_D = (0.78, 0, -0.16)$ $\mathbf{n}_E = (-0.38, 0.67, -0.16)$ $\mathbf{n}_{DE} = (-0.3, 0.13, 0)$ $\mathbf{c}_3 = (0.078, 0.14, 0.3)$	$\tau_P \mathbf{t}_D$ $+\tau_P \mathbf{t}_E$ $+\tau_{PP} \mathbf{t}_{DE}$ $= 0$
quadrilateral– pentagon 		$V_2 = (-0.66, 0, -0.45)$ $V_4 = (-0.38, -0.66, 0.2)$ $\mathbf{n}_E = (0.78, 0, -0.16)$ $\mathbf{n}_A = (0.28, 0.5, 0.55)$ $\mathbf{n}_{AE} = (-0.3, 0.3, 0.44)$ $\mathbf{c}_2 = (-0.27, 0.66, -0.65)$	$\tau_Q \mathbf{t}_A$ $+\tau_P \mathbf{t}_E$ $+\tau_{PQ} \mathbf{t}_{AE}$ $= 0$
quadrilateral– quadrilateral 		$V_1 = (0, 0, -0.79)$ $V_5 = (-0.65, 0, -0.45)$ $\mathbf{n}_A = (0.28, 0.5, 0.55)$ $\mathbf{n}_B = (-0.57, 0, 0.55)$ $\mathbf{n}_{AB} = (0, 0.52, 0)$ $\mathbf{c}_1 = (-0.66, 0, 0.35)$	$\tau_Q \mathbf{t}_A$ $+\tau_Q \mathbf{t}_B$ $+\tau_{QQ} \mathbf{t}_{AB}$ $= 0$
triangle–pentagon 		$V_3 = (-0.31, -0.53, 0.51)$ $V_7 = (-0.31, 0.53, 0.51)$ $\mathbf{n}_D = (0.78, 0, -0.16)$ $\mathbf{n}_N = (0, 0, 0.79)$ $\mathbf{n}_{DN} = (0.54, 0, 0.33)$ $\mathbf{c}_4 = (0, 1.06, 0)$	$\tau_P \mathbf{t}_D$ $+\tau_T \mathbf{t}_N$ $+\tau_{PT} \mathbf{t}_{DN}$ $= 0$

Table 3. Radial edges.

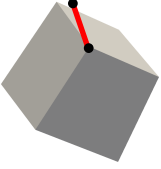
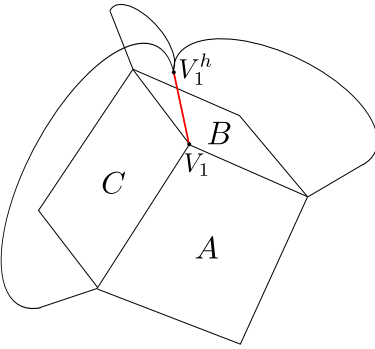
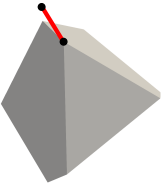
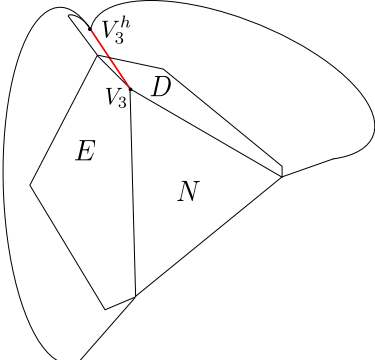
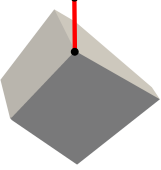
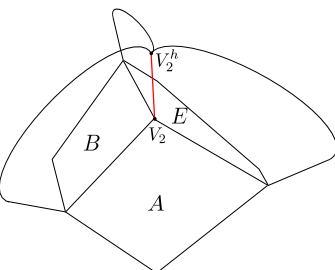
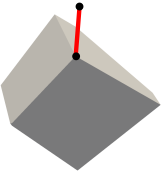
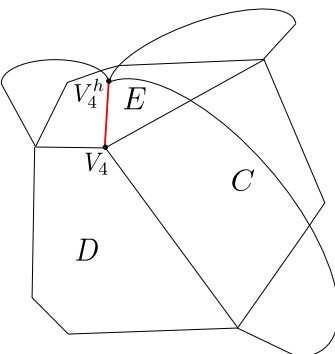
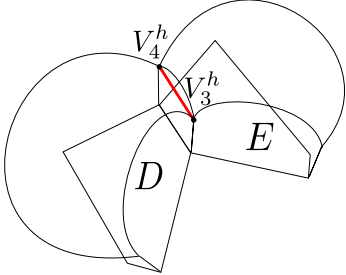
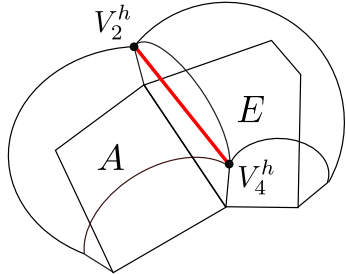
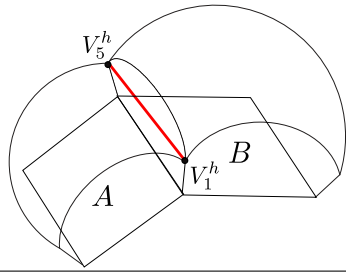
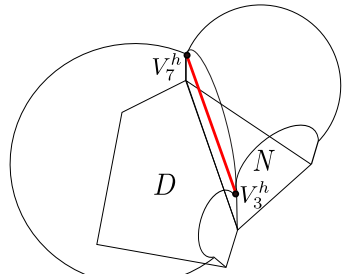
Interaction	Edges	Angles	Equation	
quadrilateral– quadrilateral– quadrilateral			$V_1^h = (0, 0, -0.79 - h_4)$ $\mathbf{n}_{AB} = (0, 0.52, 0)$ $\mathbf{n}_{BC} = (0.45, -0.26, 0)$ $\mathbf{n}_{CA} = (-0.45, -0.26, 0)$ $\mathbf{c}_5 = (0, 0, h_4)$	$\tau_{QQ} \mathbf{t}_{AB}^r$ $+ \tau_{QQ} \mathbf{t}_{BC}^r$ $+ \tau_{QQ} \mathbf{t}_{CA}^r$ $= 0$
pentagon– pentagon– triangle			$V_3^h = (-0.31 - 0.39h_3,$ $-0.53 - 0.67h_3,$ $0.51 + 0.64h_3)$ $\mathbf{n}_{DE} = (-0.3, 0.13, 0)$ $\mathbf{n}_{DN} = (-0.27, 0.47, 0.33)$ $\mathbf{n}_{EN} = (-0.54, 0, 0.33)$ $\mathbf{c}_7 = (0.39h_3, 0.67h_3, -0.64h_3)$	$\tau_{PT} \mathbf{t}_{DN}^r$ $+ \tau_{PT} \mathbf{t}_{EN}^r$ $+ \tau_{PP} \mathbf{t}_{DE}^r$ $= 0$
quadrilateral– quadrilateral– pentagon			$V_2^h = (-0.66 - 0.83h_1,$ $0,$ $-0.45 - 0.56h_1)$ $\mathbf{n}_{AB} = (0, 0.52, 0)$ $\mathbf{n}_{AE} = (-0.3, 0.31, 0.44)$ $\mathbf{n}_{BE} = (0.3, 0.31, -0.44)$ $\mathbf{c}_6 = (0.83h_1, 0, 0.56h_1)$	$\tau_{QQ} \mathbf{t}_{AB}^r$ $+ \tau_{PQ} \mathbf{t}_{AE}^r$ $+ \tau_{PQ} \mathbf{t}_{BE}^r$ $= 0$
pentagon– pentagon– quadrilateral			$V_4^h = (-0.38 - 0.48h_1,$ $-0.67 - 0.84h_1,$ $0.20 + 0.25h_1)$ $\mathbf{n}_{DE} = (-0.23, 0.13, 0)$ $\mathbf{n}_{CD} = (-0.3, 0.31, 0.44)$ $\mathbf{n}_{CE} = (0.41, -0.17, 0.44)$ $\mathbf{c}_8 = (0.48h_1, 0.84h_1, -0.25h_1)$	$\tau_{PP} \mathbf{t}_{DE}^r$ $+ \tau_{PQ} \mathbf{t}_{CD}^r$ $+ \tau_{PQ} \mathbf{t}_{CE}^r$ $= 0$

Table 4. Edges on the free surface. The expressions of \mathbf{n}_i^s are reported at the beginning of this Appendix.

Interaction	Edges	Angles	Equation
pentagon– pentagon		$\mathbf{n}_{DE} = (-0.23, 0.13, 0)$ $\mathbf{c}_{11} = (0.078 + 0.1h_3,$ $0.14 + 0.17h_3,$ $0.3 + 0.38h_3)$	$\tau_P^s \mathbf{t}_D^s$ $+\tau_P^s \mathbf{t}_E^s$ $+\tau_{PP}^s \mathbf{t}_{DE}^s$ $= 0$
quadrilateral– pentagon		$\mathbf{n}_{AE} = (0.41, -0.17, 0.44)$ $\mathbf{c}_{10} = (-0.27 - 0.34h_1,$ $0.67 + 0.84h_1,$ $-0.65 - 0.82h_1)$	$\tau_P^s \mathbf{t}_E^s$ $+\tau_Q^s \mathbf{t}_A^s$ $+\tau_{PQ}^s \mathbf{t}_{AE}^s$ $= 0$
quadrilateral– quadrilateral		$\mathbf{n}_{AB} = (0, 0.52, 0)$ $\mathbf{c}_9 = (-0.66 - 0.82h_4,$ $0,$ $0.35 + 0.44h_4)$	$\tau_Q^s \mathbf{t}_A^s$ $+\tau_Q^s \mathbf{t}_B^s$ $+\tau_{QQ}^s \mathbf{t}_{AB}^s$ $= 0$
pentagon– triangle		$\mathbf{n}_{DN} = (-0.54, 0, 0.33)$ $\mathbf{c}_{12} = (0, -1.06 - 1.34h_3, 0)$	$\tau_P^s \mathbf{t}_D^s$ $+\tau_T^s \mathbf{t}_N^s$ $+\tau_{PT}^s \mathbf{t}_{DN}^s$ $= 0$

